Graz University of Technology
Institute of Applied Mechanics

Preprint Series

Preprint No 01/2016

Convolution Quadrature for the Wave Equation with Impedance Boundary Conditions

Stefan A. Sauter
Institut für Mathematik, University Zurich

Martin Schanz
Institute of Applied Mechanics, Graz University of Technology

Published in *Journal of Computational Physics*, 334, 442–459, 2017
DOI: 10.1016/j.jcp.2017.01.013

Latest revision: 9.1.2017

Abstract

We consider the numerical solution of the wave equation with impedance boundary conditions and start from a boundary integral formulation for its discretization. We develop the generalized convolution quadrature (gCQ) to solve the arising acoustic retarded potential integral equation for this impedance problem.

For the special case of scattering from a spherical object, we derive representations of analytic solutions which allow to investigate the effect of the impedance coefficient on the acoustic pressure analytically. We have performed systematic numerical experiments to study the convergence rates as well as the sensitivity of the acoustic pressure from the impedance coefficients.

Finally, we apply this method to simulate the acoustic pressure in a building with a fairly complicated geometry and to study the influence of the impedance coefficient also in this situation.

1 Introduction

The efficient and reliable simulation of scattered waves in unbounded exterior domains is a numerical challenge and the development of *fast* numerical methods is far from being matured. We are interested in boundary integral formulations of the problem to avoid the use of an artificial boundary with approximate transmission conditions [22, 1, 10, 18, 7] and to allow for recasting the problem (under certain assumptions which will be detailed later) as an integral equation on the surface of the scatterer.

The methods for solving the arising integral equations can be split into a) *frequency domain* methods where an incident plane wave at prescribed frequency excites a scattered field and a time periodic ansatz reduces the problem to a purely spatial Helmholtz equation and b) *time-domain* methods where the excitation is allowed to have a broad temporal band width and, possibly, an a-periodic behavior with respect to time.

For the solution, an ansatz as an acoustic retarded potential integral equation (RPIE) is employed. Among the most popular methods for discretizing this equation are: a) the *convolution quadrature* (CQ) method [29, 30, 21, 28, 5, 13] and b) the direct *space-time Galerkin discretization* (see, e.g., [2, 19, 20, 39, 40, 42]).

In this paper, the *generalized convolution quadrature* (gCQ) is considered for the discretization of the RPIE. This method has been introduced in [28, 27] for the implicit Euler time method and for the Runge-Kutta method in [26]. In contrast to the original CQ method the gCQ method allows for variable time stepping.

We apply this method to the wave equation with linear impedance boundary condition (for non-linear boundary conditions we refer to [3, 17, 6]) and study the effect of different values of the impedance coefficient on the solution *analytically* for a spherical scatterer and *numerically* for concrete applications with a fairly complicated geometry.

The paper is organized as follows. In Section 2, we will introduce the wave equation with impedance conditions and the corresponding retarded potential integral equation. In Section 3, we introduce the generalized convolution quadrature method for the RPIE with impedance boundary conditions. New representations for analytic solutions in the case of a spherical scatterer are derived in Section 4 which allow for a stable numerical evaluation.

Numerical experiments are described in Section 5. First, systematic studies of the convergence order have been performed for problems where the exact solution is known and the effect of the impedance coefficient on the acoustic pressure is investigated numerically. Then, the method is applied to model the effect of the impedance coefficient for the acoustic pressure in the atrium of the "Institut für Mathematik" at the University Zurich. In 2010/11 an acoustic absorber was installed on the ceilings to improve the acoustics in the building. Our goal is to model this effect numerically by the gCQ method and the results are also described in Section 5. In the Conclusions 6 we summarize the main findings in this papers.

2 Setting

Let $\Omega^- \subset \mathbb{R}^3$ be a bounded Lipschitz domain with boundary $\Gamma := \partial\Omega$ and let $\Omega^+ := \mathbb{R}^3 \backslash \overline{\Omega^-}$ denote its unbounded complement. Let n denote the unit normal vector to Γ pointing in the exterior domain Ω^+. We consider the homogeneous wave equation (with constant sound speed c in the medium) for $\sigma \in \{+,-\}$

$$\begin{aligned} \partial_{tt}u - c^2\Delta u &= 0 \quad \text{in } \Omega^\sigma \times \mathbb{R}_{>0}, \\ u(x,0) = \partial_t u(x,0) &= 0 \quad \text{in } \Omega^\sigma, \\ \gamma_1^\sigma(u) - \sigma\tfrac{\alpha}{c}\gamma_0^\sigma(\partial_t u) &= f \quad \text{on } \Gamma \times \mathbb{R}_{>0}, \end{aligned} \tag{1}$$

where $\gamma_1^\sigma = \partial/\partial n$ is the normal derivative applied to a sufficiently smooth function in Ω^σ and γ_0^σ denotes the trace operator to Γ applied to a sufficiently smooth function in Ω^σ. If the domain $\Omega \in \{\Omega^-,\Omega^+\}$ is clear from the context we skip the superscript σ and simply write γ_1 and γ_0. In (1), α denotes the non-negative admittance, which is the inverse of the specific impedance function of the surface Γ. Specific means that the impedance is scaled by the density and the wave velocity. The value of α is mathematically non-negative, however, realistic values are in the range $0 \leq \alpha \leq 1$. The lower limit models a sound hard wall and the upper limit is a totally absorbing surface. Further, measured values show a frequency dependence and are listed in national regulations like the ÖNORM in Austria (ÖNORM EN 12354-6).

Such kind of absorbing boundary condition is a simple possible choice to model the absorption of a surface. The generalization to frequency depending admittance leads to the boundary condition $\gamma_1^\sigma(u) - \sigma\frac{\alpha}{c} * \gamma_0^\sigma(\partial_t u) = f(x,t)$, where * denotes the convolution with respect to time. We emphasize that the (generalized) convolution quadrature can handle this case without significant modifications (see, e.g., [8]). Certainly, more complicated models exist which takes higher derivatives into account. The most realistic models consider an absorbing layer of porous material on the real surface, which is the computational most expensive way (see, e.g., [15, 35]). Here, this simple model is used as it is common in real world applications.

2.1 Layer Potentials

We employ layer potentials to express the solution in terms of retarded potentials (cf. [43, 16, 2, 41]). The ansatz for the solution u as a single layer potential is given by

$$u(x,t) = (\mathcal{S} * \varphi)(x,t) := \int_\Gamma \frac{\varphi\left(y, t - \frac{\|x-y\|}{c}\right)}{4\pi\|x-y\|} d\Gamma_y \qquad \forall (x,t) \in \Omega^\sigma \times \mathbb{R}_{>0},$$

which satisfies the first two equations in (1). The density φ then is determined via the third equation. Alternatively we can represent the solution as a double layer potential

$$\begin{aligned} u(x,t) = (\mathcal{D} * \psi)(x,t) &:= \int_\Gamma \left(\frac{\partial}{\partial n(y)} \frac{\psi\left(z, t - \frac{\|x-y\|}{c}\right)}{4\pi\|x-y\|} \right)\Bigg|_{z=y} d\Gamma_y \\ &= \frac{1}{4\pi}\int_\Gamma \frac{\langle n(y), x-y\rangle}{\|x-y\|^2} \left(\frac{\psi\left(y, t - \frac{\|x-y\|}{c}\right)}{\|x-y\|} + \frac{1}{c}\partial_t \psi\left(y, t - \frac{\|x-y\|}{c}\right) \right) d\Gamma_y. \end{aligned}$$

The application of the trace γ_0 and normal trace γ_1 to u involves the following boundary integral operators

$$
\begin{aligned}
(\mathcal{V}*\varphi)(x,t) &= \int_\Gamma \frac{\varphi\left(y,t-\frac{\|x-y\|}{c}\right)}{4\pi\|x-y\|} d\Gamma_y,\\
(\mathcal{K}*\psi)(x,t) &= \frac{1}{4\pi}\int_\Gamma \frac{\langle n(y),x-y\rangle}{\|x-y\|^2}\left(\frac{\psi\left(y,t-\frac{\|x-y\|}{c}\right)}{\|x-y\|}+\frac{\partial_t\psi\left(y,t-\frac{\|x-y\|}{c}\right)}{c}\right) d\Gamma_y,\\
\left(\mathcal{K}'*\varphi\right)(x,t) &= \frac{1}{4\pi}\int_\Gamma \frac{\langle n(x),y-x\rangle}{\|x-y\|^2}\left(\frac{\varphi\left(y,t-\frac{\|x-y\|}{c}\right)}{\|x-y\|}+\frac{\partial_t\varphi\left(y,t-\frac{\|x-y\|}{c}\right)}{c}\right) d\Gamma_y,\\
(\mathcal{W}*\psi)(x,t) &= -\frac{\partial}{\partial n(x)}(\mathcal{D}*\psi)(x,t)
\end{aligned}
$$

for almost all $(x,t)\in\Gamma\times\mathbb{R}_{>0}$, more precisely, for all $(x,t)\in\Gamma\times\mathbb{R}_{>0}$, where Γ is smooth in a neighborhood of x. Then, it holds for $\sigma\in\{+,-\}$

$$
\begin{aligned}
\gamma_0^\sigma(\mathcal{S}*\varphi) &= (\mathcal{V}*\varphi),\\
\gamma_1^\sigma(\mathcal{S}*\varphi) &= -\left(\sigma\frac{\varphi}{2}-\mathcal{K}'*\varphi\right),\\
\gamma_0^\sigma(\mathcal{D}*\psi) &= \sigma\frac{\psi}{2}+\mathcal{K}*\psi\\
-\gamma_1^\sigma(\mathcal{D}*\psi) &= \mathcal{W}*\psi,
\end{aligned}
$$

where, again, these equations hold almost everywhere on $\Gamma\times\mathbb{R}_{>0}$.

The third equation in (1) leads to the boundary integral equation for the single layer ansatz

$$
-\left(\sigma\frac{\varphi}{2}-\mathcal{K}'*\varphi\right)-\sigma\frac{\alpha}{c}(\mathcal{V}*\partial_t\varphi)=f \quad \text{a.e. in } \Gamma\times\mathbb{R}_{>0}. \tag{2}
$$

The double layer ansatz leads to the boundary integral equation

$$
-\mathcal{W}*\psi-\frac{\sigma\alpha}{c}\left(\sigma\frac{\partial_t\psi}{2}+\mathcal{K}*\partial_t\psi\right)=f \quad \text{a.e. in } \Gamma\times\mathbb{R}_{>0}. \tag{3}
$$

3 Generalized Convolution Quadrature (gCQ)

The convolution quadrature method has been developed by Lubich, see [29, 30, 31, 33, 32] for parabolic and hyperbolic problems. The idea is to express the RPIE as the inverse Laplace transform applied to the counterpart of the RPIE in the Fourier-Laplace domain which reduces the problem to the solution of a scalar ODE of the form $y'=sy+g$, for s being the variable in the Laplace domain. The temporal discretization then is based on the numerical approximation of the solution of this ODE by some time-stepping method and the transformation of the resulting equation back to the original time domain.

The original CQ method requires constant time stepping. However, if the right-hand side is not uniformly smooth and/or contains non-uniformly distributed variations in time, and/or consists of localized pulses, the use of adaptive time stepping becomes very important in order to keep the number of time steps reasonably small. The *generalized convolution quadrature* (gCQ) has been introduced in [28, 27, 26] and allows for variable time stepping.

We recall the definition of the Laplace transform and its inverse

$$\begin{aligned}
\hat{f}(s) &:= \mathcal{L}(f)(s) := \int_0^\infty \mathrm{e}^{-st} f(t)\,dt \\
f(t) &:= \frac{1}{2\pi \mathrm{i}} \int_\gamma \mathrm{e}^{st} \hat{f}(s)\,ds \quad \text{for } \gamma := \rho + \mathrm{i}\,\mathbb{R} \text{ and some } \rho > 0
\end{aligned}$$

for a Laplace-transformable function f, where the vertical contour γ runs from $\rho - \mathrm{i}\infty$ to $\rho + \mathrm{i}\infty$. The Laplace transformed boundary integral operators are given for sufficiently smooth functions $\Phi, \Psi : \Gamma \to \mathbb{C}$ by (cf. [43], [41])[1]

$$\begin{aligned}
\widehat{\mathcal{S}}(s)\Phi(x) &= \int_\Gamma \frac{\mathrm{e}^{-s\|x-y\|/c}}{4\pi\|x-y\|}\Phi(y)\,d\Gamma_y && \forall x \in \Omega^\sigma \quad \forall s \in \mathbb{C}_\rho, \\
\widehat{\mathcal{D}}(s)\Psi(x) &= \int_\Gamma \frac{\mathrm{e}^{-s\|x-y\|/c}\langle n(y), x-y\rangle}{4\pi\|x-y\|^2}\left(\frac{1}{\|x-y\|} + \frac{s}{c}\right)\Psi(y)\,d\Gamma_y && \forall x \in \Omega^\sigma \quad \forall s \in \mathbb{C}_\rho, \\
\widehat{\mathcal{V}}(s)\Phi(x) &= \int_\Gamma \frac{\mathrm{e}^{-s\|x-y\|/c}}{4\pi\|x-y\|}\Phi(y)\,d\Gamma_y && \forall x \in \Gamma \quad \forall s \in \mathbb{C}_\rho, \\
\widehat{\mathcal{K}}(s)\Psi(x) &= \int_\Gamma \frac{\mathrm{e}^{-s\|x-y\|/c}\langle n(y), x-y\rangle}{4\pi\|x-y\|^2}\left(\frac{1}{\|x-y\|} + \frac{s}{c}\right)\Psi(y)\,d\Gamma_y && \forall x \in \Gamma \quad \forall s \in \mathbb{C}_\rho, \\
\widehat{\mathcal{K}'}(s)\Phi(x) &= \int_\Gamma \frac{\mathrm{e}^{-s\|x-y\|/c}\langle n(x), y-x\rangle}{4\pi\|x-y\|^2}\left(\frac{1}{\|x-y\|} + \frac{s}{c}\right)\Phi(y)\,d\Gamma_y && \forall x \in \Gamma \quad \forall s \in \mathbb{C}_\rho, \\
\widehat{\mathcal{W}}(s)\Psi(x) &= -\frac{\partial}{\partial n(x)}\widehat{\mathcal{D}}(s)\Psi(x) && \forall x \in \Gamma \quad \forall s \in \mathbb{C}_\rho,
\end{aligned}$$

where

$$\mathbb{C}_\rho := \{s \in \mathbb{C} \mid \operatorname{Re} s \geq \rho\} \quad \text{for some } \rho > 0. \tag{4}$$

The definition of the (generalized) convolution quadrature depends of the growth behavior of the inverse Laplace transformed integral operator with respect to the frequency variable. This operator must decay fast enough such that the integral over the infinite contour γ exists. In our case this requires a regularization parameter $\mu \in \mathbb{N}_0$ which will be specified later. We denote by $f^{(\mu)}$ as usual the μ-th derivative of f. For $\mu \in \mathbb{Z}$, we define

$$\widehat{\mathcal{V}}_\mu(s) := s^{-\mu}\widehat{\mathcal{V}}(s) \tag{5}$$

[1] In fact these operators are well defined for all $s \in \mathbb{C}$ with $\operatorname{Re} s > 0$. However, we employ the positive parameter ρ in order to express bounds of the inverse operators in terms of $\rho > 0$.

while $\widehat{\mathcal{K}_\mu}$, $\widehat{\mathcal{K}'}_\mu$, $\widehat{\mathcal{W}_\mu}$ and other frequency dependent integral operators are defined analogously.

The application of the inverse Laplace transform to (2) leads to the following integro-differential equation in the frequency domain

$$\frac{1}{2\pi \mathrm{i}} \int_\gamma \left(\widehat{Q^\sigma}\right)_{-\mu}(s)\, U(s,t)\, ds = f^{(\mu)}(t), \tag{6a}$$

$$\partial_t U(s,t) = sU(s,t) + \Phi, \qquad U(s,0) = 0, \tag{6b}$$

$$\text{with} \quad \widehat{Q^\sigma}(s) := -\left(\frac{\sigma}{2} I - \widehat{\mathcal{K}'}(s)\right) - \sigma \frac{\alpha}{c} s \widehat{\mathcal{V}}(s), \tag{6c}$$

where we have suppressed the x-dependence of the functions and operators in the notation.

The same technique can be applied to (3) and we obtain

$$\frac{1}{2\pi \mathrm{i}} \int_\gamma \left(\widehat{R^\sigma}\right)_{-\mu}(s)\, V(s,t)\, ds = f^{(\mu)} \tag{7a}$$

$$\partial_t V(s,t) = sV(s,t) + \Psi, \qquad V(s,0) = 0, \tag{7b}$$

$$\text{with} \quad \widehat{R^\sigma}(s) := -\widehat{\mathcal{W}}(s) - \frac{\alpha}{c} s \left(\frac{1}{2} I + \sigma \widehat{\mathcal{K}}(s)\right). \tag{7c}$$

The operators $\widehat{Q^\sigma}(s)$ and $\widehat{R^\sigma}(s)$ are continuous and invertible in appropriate Sobolev spaces $H^\mu(\Gamma)$ on the surface Γ and have algebraic growth behavior with respect to $|s|$. Since the growth exponent will be a control parameter for the generalized convolution quadrature, we provide here the relevant theorem. We restrict here to positive and bounded admittance α to express the continuity constant of the integral operators and their inverses in a simple way by its lower and upper bound. Generalizations to more general admittance functions are possible but lie outside the scope of this paper.

Theorem 3.1. Let $\rho > 0$ in (4) and $\rho_1 := \min\{1, \rho\}$. Let the admittance function satisfy

$$0 < \alpha_{\min} := \min_{x\in\Gamma} \alpha(x) \leq \max_{x\in\Gamma} \alpha(x) =: \alpha_{\max} < \infty.$$

Then, the operators $\widehat{Q^\sigma}(s)$ and $\widehat{R^\sigma}(s)$ and their inverses satisfy the following continuity estimates for all $s \in \mathbb{C}_\rho$

$$\left\|\widehat{Q^\sigma}(s)\right\|_{H^{-1/2}(\Gamma)\leftarrow H^{-1/2}(\Gamma)} \leq C_1 \left(C_2 + \frac{\alpha_{\max}}{c}\right)|s|^2, \tag{8a}$$

$$\left\|\widehat{R^\sigma}(s)\right\|_{H^{-1/2}(\Gamma)\leftarrow H^{1/2}(\Gamma)} \leq C_1 \left(C_2 + \frac{\alpha_{\max}}{c}\right)|s|^{5/2}, \tag{8b}$$

and

$$\left\|\widehat{Q^\sigma}^{-1}(s)\right\|_{H^{-1/2}(\Gamma)\leftarrow H^{-1/2}(\Gamma)} \leq C_1 \frac{c}{\alpha_{\min}} |s|, \tag{9a}$$

$$\left\|\widehat{R^\sigma}^{-1}(s)\right\|_{H^{-1/2}(\Gamma)\leftarrow H^{1/2}(\Gamma)} \leq C_2 |s|^2. \tag{9b}$$

The constants C_1, C_2 only depend on ρ and ρ_1.

Proof. The operator $\widehat{Q^{\sigma}}(s)$ and $\widehat{R^{\sigma}}(s)$ can be expressed in terms of the Dirichlet-to-Neumann map DtN^{σ} and the Neumann-to-Dirichlet map NtD^{σ} for the exterior $(\sigma = 1)$ and the interior $(\sigma = -1)$ domain Ω^{σ}. It holds (cf. [24, Appendix 2])

$$\widehat{Q^{\sigma}}(s) = -\sigma\left(-\sigma\,\mathrm{DtN}^{\sigma} + \frac{\alpha}{c}sI\right)\widehat{\mathcal{V}}(s),$$
$$\widehat{R^{\sigma}}(s) = -\left(I - s\frac{\alpha}{c}\sigma\,\mathrm{NtD}^{\sigma}\right)\widehat{\mathcal{W}}(s).$$

For the continuity estimates we employ the representations (6c) and (7c) and well known continuity estimates for $\widehat{\mathcal{K}}$, $\widehat{\mathcal{K}'}$, $\widehat{\mathcal{V}}$, $\widehat{\mathcal{W}}$ (see, e.g., [2, Prop. 3], [14, formulae (10), (11)], [24, Appendix 2]) to obtain

$$\left\|\widehat{Q^{\sigma}}(s)\right\|_{H^{-1/2}(\Gamma)\leftarrow H^{-1/2}(\Gamma)} \le \frac{1}{2} + C\frac{|s|^{3/2}}{\rho\rho_1^{3/2}} + C\frac{\alpha_{\max}}{c}\frac{|s|^2}{\rho\rho_1^2},$$
$$\left\|\widehat{R^{\sigma}}(s)\right\|_{H^{-1/2}(\Gamma)\leftarrow H^{1/2}(\Gamma)} \le C\frac{|s|^2}{\rho\rho_1} + \frac{\alpha_{\max}}{c}|s|\left(\frac{1}{2} + C\frac{|s|^{3/2}}{\rho\rho_1^{3/2}}\right)$$

for all $s \in \mathbb{C}_{\rho}$. From this, estimates (8) follow by using $|s| \ge \operatorname{Re} s \ge \rho$.

For the inverses we employ [24, Prop. 17, 18]:

$$\operatorname{Re}\left(\mathrm{e}^{-\mathrm{i}\operatorname{Arg} s}\left(\Phi, \left(-\sigma\,\mathrm{DtN}^{\sigma} + \frac{\alpha}{c}sI\right)\Phi\right)_{L^2(\Gamma)}\right) \ge \left(C\frac{\rho\rho_1^2}{|s|} + \frac{\alpha_{\min}}{c}|s|\right)\|\Phi\|^2_{H^{1/2}(\Gamma)} \quad \forall\Phi \in H^{1/2}(\Gamma),$$
$$\operatorname{Re}\left(\mathrm{e}^{\mathrm{i}\operatorname{Arg} s}\left(\Psi, \left(I - s\frac{\alpha}{c}\sigma\,\mathrm{NtD}^{\sigma}\right)\Psi\right)_{L^2(\Gamma)}\right) \ge \left(\operatorname{Re} s + C\frac{\alpha_{\min}}{c}\rho\rho_1\right)\frac{1}{|s|}\|\Psi\|^2_{H^{-1/2}(\Gamma)} \quad \forall\Psi \in H^{-1/2}(\Gamma).$$

The Lax-Milgram lemma implies

$$\left\|\left(-\sigma\,\mathrm{DtN}^{\sigma} + \frac{\alpha}{c}sI\right)^{-1}\right\|_{H^{-1/2}(\Gamma)\leftarrow H^{1/2}(\Gamma)} \le \frac{|s|}{C\rho\rho_1^2 + \frac{\alpha_{\min}}{c}|s|^2}$$
$$\left\|\left(I - s\frac{\alpha}{c}\sigma\,\mathrm{NtD}^{\sigma}\right)^{-1}\right\|_{H^{-1/2}(\Gamma)\leftarrow H^{-1/2}(\Gamma)} \le \frac{|s|}{C\frac{\alpha_{\min}}{c}\rho\rho_1 + \operatorname{Re} s}.$$

The combination with well known mapping properties of $\widehat{\mathcal{V}}^{-1}$ and $\widehat{\mathcal{W}}^{-1}$ (cf. [24, Prop. 16, 19]) leads to

$$\left\|\widehat{Q^{\sigma}}^{-1}(s)\right\|_{H^{-1/2}(\Gamma)\leftarrow H^{-1/2}(\Gamma)} \le \left\|\widehat{\mathcal{V}}^{-1}(s)\right\|_{H^{-1/2}(\Gamma)\leftarrow H^{1/2}(\Gamma)}\left\|\left(-\sigma\,\mathrm{DtN}^{\sigma} + \frac{\alpha}{c}sI\right)^{-1}\right\|_{H^{-1/2}(\Gamma)\leftarrow H^{1/2}(\Gamma)}$$
$$\le C\frac{|s|^2}{\rho\rho_1}\frac{|s|}{C\rho\rho_1^2 + \frac{\alpha_{\min}}{c}|s|^2},$$
$$\left\|\widehat{R^{\sigma}}^{-1}(s)\right\|_{H^{-1/2}(\Gamma)\leftarrow H^{1/2}(\Gamma)} \le \left\|\widehat{\mathcal{W}}^{-1}(s)\right\|_{H^{1/2}(\Gamma)\leftarrow H^{-1/2}(\Gamma)}\left\|\left(I - s\frac{\alpha}{c}\sigma\,\mathrm{NtD}^{\sigma}\right)^{-1}\right\|_{H^{-1/2}(\Gamma)\leftarrow H^{-1/2}(\Gamma)}$$
$$\le C\frac{|s|}{\rho\rho_1^2}\frac{|s|}{C\frac{\alpha_{\min}}{c}\rho\rho_1 + \operatorname{Re} s}$$

from which the estimates of the inverse operator follow. $\square$

Remark 1. According to the growth of the inverse Laplace transformed integral operators $\widehat{Q^\sigma}^{-1}(s)$, $\widehat{R^\sigma}^{-1}(s)$ we define

$$\mu := \begin{cases} 3 & \text{for problem (2),} \\ 4 & \text{for problem (3).} \end{cases}$$

This definition implies that the contour integrals $\int_\gamma \left(\widehat{Q^\sigma}^{-1}\right)_\mu (s)\, ds$ and $\int_\gamma \left(\widehat{R^\sigma}^{-1}\right)_\mu (s)\, ds$ exist. The choice of $\mu > 0$ has theoretical reasons and ensures that the inverse Laplace transform of the operators exists as a contour integral in the Riemann sense. In numerical experiments one observes that the choice $\mu = 0$ does not spoil the accuracy of the solution so that the condition $\mu > 0$ might be a result of an artifact in the error analysis via the inverse Laplace transform.

By approximating the ODE in (6b) and (7b), by a time stepping scheme and replacing the integral $\int_\gamma \ldots$ by a contour quadrature leads to the approximation of (2) and (3) by generalized convolution quadrature. The following algorithm is taken from [27] and employs the implicit Euler method for discretizing the ODEs in (6b), (7b); for a generalization to Runge-Kutta methods we refer to [26]. Let time steps $(t_j)_{j=0}^N$ be given

$$0 = t_0 < t_1 < \ldots < t_N = T$$

and introduce the corresponding mesh sizes $\Delta_j = t_j - t_{j-1}$ The implicit Euler method for solving (6b) defines approximations $U_n(s) \approx U(s, t_n)$ by

$$U_n = \frac{U_{n-1}}{1 - s\Delta_n} + \frac{\Delta_n \Phi_n}{1 - s\Delta_n}, \qquad U_0 = 0.$$

Inserting this into (6a) at time t_n and using Cauchy's integral theorem results in

$$\left(\widehat{Q^\sigma}\right)_{-\mu} \left(\frac{1}{\Delta_n}\right) \Phi_n = f^{(\mu)}(t_n) - \frac{1}{2\pi \mathrm{i}} \int_{\mathcal{C}} \frac{\left(\widehat{Q^\sigma}\right)_{-\mu}(s)}{1 - s\Delta_n} U_{n-1}(s)\, ds. \tag{10}$$

Here, $\mathcal{C}$ is a bounded contour which encircles all poles $\left(\Delta_m^{-1}\right)_{m=1}^N$ of the integrand and is clockwise oriented (cf. [27]).

In [25, 27] a quadrature rule for the contour integral in (10) has been developed and analyzed. Denote by $s_\ell \in \mathcal{C}$ the nodes and by w_ℓ the weights, $\ell = 1, \cdots, N_Q$. By replacing the integral $\int_{\mathcal{C}} \ldots$ by the quadrature formula, we can formulate the generalized convolution quadrature in an algorithmic way.

Definition 3.2 (gCQ). The generalized convolution quadrature for solving (6), (7) is given by the procedure: For $n = 1, \ldots, N$ do

$$U_{n-1}(s_\ell) := \left\{ \begin{array}{ll} 0 & n = 1, \\ \frac{U_{n-2}(s_\ell)}{1 - \Delta_{n-1} s_\ell} + \frac{\Delta_{n-1}}{1 - \Delta_{n-1} s_\ell} \Lambda_{n-1} & n \geq 2 \end{array} \right\} \quad \ell = 1, \ldots N_Q \tag{11a}$$

$$Z\left(\frac{1}{\Delta_n}\right) \Lambda_n := f^{(\mu)}(t_n) - \sum_{\ell=1}^{N_Q} w_\ell \frac{Z(s_\ell)}{1 - s_\ell \Delta_n} U_{n-1}(s_\ell)\, ds, \tag{11b}$$

where $\Lambda_n := \Phi_n$ and $Z := \left(\widehat{Q^\sigma}\right)_{-\mu}$ for problem (6) and $\Lambda_n := \Psi_n$ and $Z := \left(\widehat{R^\sigma}\right)_{-\mu}$ for problem (7).

Remark 2. We have presented the gCQ method for the time discretization of the wave equation with impedance boundary conditions. To obtain a fully discrete equation the boundary integral operators in (10) have to be discretized, e.g., by a standard Galerkin boundary element method. This is described, e.g., in [28]. The error analysis for the temporal discretization requires solely the quantitative knowledge of the polynomial growth behavior of the operators in Theorem 3.1 with respect to the frequency variable while the error analysis for the fully discrete equation has been developed in [28]. In this light, the main focus in this paper is on the numerical realization and some systematic convergence studies.

4 Analytic Solutions

In this section, we provide sample solutions for the wave equation with impedance boundary conditions on the sphere. This allows to study explicitly the influence on the admittance function α on the acoustic pressure and to compare the numerical solution with an exact solution.

There are essentially two different ways for the construction of exact reference solutions for boundary integral equations. One way is to employ Kirchhoff's formulae (see, e.g., [41]) for the wave equation (2), (3) in the Laplace domain which can be combined such that we get the relations

$$\widehat{Q^-}(s)\,\gamma_1^+\widehat{u}^+ = \widehat{R^-}(s)\,\gamma_0^+\widehat{u}^+,$$
$$\widehat{Q^+}(s)\,\gamma_1^-\widehat{u}^- = \widehat{R^+}(s)\,\gamma_0^-\widehat{u}^-$$

valid for homogeneous interior and exterior solutions u^-, u^+ of the wave equation in the Laplace domain. Such solutions can be created by a source distribution located outside the computational domain

$$u^-(x) := \frac{\mathrm{e}^{-s\|x-y\|/c}}{4\pi\|x-y\|} \quad \text{for fixed } y\in\Omega^+ \quad \text{and} \quad u^+(x) := \frac{\mathrm{e}^{-s\|x-y\|/c}}{4\pi\|x-y\|} \text{ for fixed } y\in\Omega^-$$

and allow to derive sample solutions for all equations $\widehat{Q^\sigma}(s)\,\Phi = \widehat{f}$ and $\widehat{R^\sigma}(s)\,\Psi = \widehat{f}$, where $\widehat{f}$ is then defined as the application of one of the integral operators $\widehat{Q^\sigma}$, $\widehat{R^\sigma}$ to the trace or normal trace of $\widehat{u}$.

Another approach can be applied for the sphere since the eigenpairs of the boundary integral operator for the acoustic single layer operator are known. From this, we will derive the eigensolutions of the time-space integral equation for the retarded acoustic single layer potential. In this case, the right-hand side is not defined as the application of an integral operator to a trace but known explicitly. In addition, this approach allows to study the behavior of the solution for higher eigenmodes and regularity issues although this study is beyond the scope of this paper. For pure Dirichlet and Neumann problems, such sample solutions have been derived, e.g., in [38] and [44].

Let $\Omega\subset\mathbb{R}^3$ denote the unit ball with surface $\Gamma := \mathbb{S}_2$. Let Y_n^m denote the spherical harmonics. We assume that the right-hand side f is given by

$$f(x,t) := f(t)\,Y_n^m(x) \tag{12}$$

with a slight abuse of notation. Note that the spherical harmonics are eigenfunctions of the boundary integral operators $\widehat{\mathcal{V}}, \widehat{\mathcal{K}}, \widehat{\mathcal{K}'}, \widehat{\mathcal{W}}$, i.e.,

$$\widehat{Z}Y_n^m = \lambda_n^{(Z)}\left(\frac{s}{c}\right)Y_n^m \quad \text{for } Z \in \left\{\mathcal{V}, \mathcal{K}, \mathcal{K}', \mathcal{W}\right\}.$$

Explicitly it holds (cf. [23, 36])[2]

$$\lambda_n^{(\mathcal{V})}(s) = -s j_n(\mathrm{i}s)h_n^{(1)}(\mathrm{i}s), \qquad \lambda_n^{(\mathcal{K})}(s) = \tfrac{1}{2} - \mathrm{i}s^2 j_n(\mathrm{i}s)\partial h_n^{(1)}(\mathrm{i}s),$$

$$\lambda_n^{(\mathcal{W})}(s) = -s^3\partial j_n(\mathrm{i}s)\partial h_n^{(1)}(\mathrm{i}s), \qquad \lambda_n^{(\mathcal{K}')}(s) = \lambda_n^{(\mathcal{K})}(s),$$

with the spherical Bessel and Hankel functions j_n, $h_n^{(1)}$ (cf. [9, §10.4.7]) and ∂j_n, $\partial h_n^{(1)}$ denoting their first derivatives. Then the Laplace transformed equations (2), (3) take the form (by using the ansatz $\varphi = \varphi(t)Y_n^m$ and $\psi = \psi(t)Y_n^m$)

$$\begin{aligned} \widehat{\varphi_n} &= \eta_n^{-1}\left(\alpha, \tfrac{s}{c}\right)\widehat{f}(s) \quad \text{with} \quad \eta_n(\alpha,s) := -\left(\tfrac{\sigma}{2} - \lambda_n^{(\mathcal{K})}(s)\right) - \sigma\alpha s\lambda_n^{(\mathcal{V})}(s), \\ \widehat{\psi_n} &= \gamma_n^{-1}\left(\alpha, \tfrac{s}{c}\right)\widehat{f}(s) \quad \text{with} \quad \gamma_n(\alpha,s) := -\lambda_n^{(\mathcal{W})}(s) - \alpha s\left(\tfrac{1}{2} + \sigma\lambda_n^{(\mathcal{K})}(s)\right). \end{aligned} \tag{13}$$

4.1 The Case $n = 0$

For $n = 0$, we have

$$\lambda_0^{(\mathcal{V})}(s) = \tfrac{1-\mathrm{e}^{-2s}}{2s}, \qquad \lambda_0^{(\mathcal{K})}(s) = \tfrac{1}{2} + \tfrac{\mathrm{e}^{-2s}-1}{2s}(s+1)$$

$$\lambda_0^{(\mathcal{W})}(s) = (1+s)\tfrac{s-1+\mathrm{e}^{-2s}(1+s)}{2s}, \qquad \lambda_0^{(\mathcal{K}')}(s) = \lambda_n^{(\mathcal{K})}(s).$$

For the reciprocal symbols η_0^{-1}, γ_0^{-1} we obtain

$$\begin{aligned} \eta_0^{-1}(\alpha,s) &:= -\frac{2s}{\sigma s(1+\alpha)+1-\mathrm{e}^{-2s}(s(1+\sigma\alpha)+1)} \\ &= -\frac{2s}{\sigma s(1+\alpha)+1}\sum_{\ell=0}^{\infty}\left(\frac{(s(1+\sigma\alpha)+1)\mathrm{e}^{-2s}}{\sigma s(1+\alpha)+1}\right)^{\ell}, \\ \gamma_0^{-1}(\alpha,s) &:= -\frac{2s}{(1+\alpha)s^2-\sigma\alpha s-1+\mathrm{e}^{-2s}(s+1)(s(\sigma\alpha+1)+1)} \\ &= -\frac{2s}{(1+\alpha)s^2-\sigma\alpha s-1}\sum_{\ell=0}^{\infty}(-1)^{\ell}\left(\frac{(s+1)((\sigma\alpha+1)s+1)\mathrm{e}^{-2s}}{(1+\alpha)s^2-\sigma\alpha s-1}\right)^{\ell}. \end{aligned}$$

[2] Note that in [36, (2.6.116)] is a misprint. For the Wronskian $\mathfrak{W}$ of the spherical Bessel functions j_ℓ, $h_\ell^{(1)}$, it holds

$$\mathfrak{W}\left(h_\ell^{(1)}(z), j_\ell(z)\right) = -\frac{\mathrm{i}}{z^2}$$

so that in [36, (3.2.22)] on the right-hand side a factor i is missing. By the same reason a factor i is also missing in the formulae [36, (3.2.23), (3.2.24)], while in formula [36, (3.2.26)] a factor i is missing only in front of the first term in the bracket. Note also that our definition of $\mathcal{W}$ differs from the definition [36, (3.2.17)] by a sign.

4.1.1 Single Layer Ansatz, exterior problem

We restrict for the analytic considerations to the exterior problem and to formulation (2).

For the exterior problem $\sigma = +$, we get

$$\eta_0^{-1}(\alpha, s) = -\frac{2s}{s(1+\alpha)+1} \sum_{\ell=0}^{\infty} \mathrm{e}^{-2\ell s}.$$

The inverse Laplace transform of this function is given by [11, 4.1(4) with $a = 1$ and $b = 2\ell$]

$$\mathcal{L}^{-1}\left(\eta_0^{-1}(\alpha, \bullet)\right)(t) = -\sum_{\ell=0}^{\infty} H(t-2\ell)\, \mathcal{L}^{-1}\left(\frac{2\bullet}{\bullet(1+\alpha)+1}\right)(t-2\ell).$$

We have

$$\mathcal{L}^{-1}\left(\frac{2\bullet}{\bullet(1+\alpha)+1}\right)(t) = \frac{2}{1+\alpha}\mathcal{L}^{-1}\left(1 - \frac{1}{1+\alpha}\frac{1}{s+\frac{1}{1+\alpha}}\right)(t) \overset{[11,\,5.2(1)]}{=} \frac{2}{1+\alpha}\left(\delta_0(t) - \frac{\mathrm{e}^{-\frac{t}{1+\alpha}}}{1+\alpha}\right)$$

with the Dirac delta distribution δ_0 so that

$$\mathcal{L}^{-1}\left(\eta_0^{-1}(\alpha, \bullet)\right)(t) = -\frac{2}{1+\alpha} \sum_{\ell=0}^{\infty} H(t-2\ell)\left(\delta_0(t-2\ell) - \frac{\mathrm{e}^{-\frac{t-2\ell}{1+\alpha}}}{1+\alpha}\right). \tag{14}$$

Hence, the density for the single layer ansatz for the exterior problem is given by[3]

$$\varphi^{+}(t) = -\frac{2}{1+\alpha} \sum_{\ell=0}^{\lfloor ct/2 \rfloor} \left(f\left(t - \frac{2\ell}{c}\right) - \frac{c}{1+\alpha} \int_0^{t-2\ell/c} \mathrm{e}^{-\frac{c(t-\tau)-2\ell}{1+\alpha}} f(\tau)\, d\tau\right) \tag{15}$$

with the notation $\lfloor x \rfloor$ for the largest integer less than or equal to x.

Example 4.1 (bump functions).

a. **General bump function.** For $\rho > 1$ and $\upsilon > 0$, we choose f in (2) as the bump function

[3] Let $\kappa > 0$. Then $\mathcal{L}^{-1}\left(\hat{f}\left(\frac{\cdot}{\kappa}\right)\right)(t) = \kappa\left(\mathcal{L}^{-1}(f)\right)(\kappa t)$ (see [11, 4.1(4) with $a = \kappa$, $b = 0$.]). Also note that $\int_{\mathbb{R}} \delta_0(\kappa t - a) = \frac{1}{\kappa}\delta_0\left(\frac{a}{\kappa}\right)$.

$f_\upsilon(t) := \left(\frac{c\rho t}{1+\alpha}\right)^\upsilon \mathrm{e}^{-\frac{c\rho t}{1+\alpha}}$. Then, the density in (15) can be written in the form[4]

$$\varphi^+(t) = -\frac{2\rho^\upsilon}{1+\alpha}\sum_{\ell=0}^{\lfloor ct/2\rfloor}\left(\left(\frac{ct-2\ell}{1+\alpha}\right)^\upsilon \mathrm{e}^{-\frac{\rho}{1+\alpha}(ct-2\ell)} - \mathrm{e}^{-\frac{ct-2\ell}{1+\alpha}}\frac{\gamma\left(\upsilon+1, \frac{(\rho-1)}{1+\alpha}(ct-2\ell)\right)}{(\rho-1)^{\upsilon+1}}\right). \tag{17}$$

b. For $f_\upsilon(t) = (ct)^\upsilon \mathrm{e}^{-ct}$ it holds

$$\varphi^+(t) = -\frac{2}{1+\alpha}\sum_{\ell=0}^{\lfloor ct/2\rfloor}\left((ct-2\ell)^\upsilon \mathrm{e}^{-(ct-2\ell)} - \frac{(1+\alpha)^\upsilon}{\alpha^{\upsilon+1}}\gamma\left(\upsilon+1, \frac{\alpha}{1+\alpha}(ct-2\ell)\right)\mathrm{e}^{-\frac{ct-2\ell}{1+\alpha}}\right). \tag{18}$$

4.2 The Solution of the Wave Equation in Ω^σ

The Laplace transformed solution of the boundary integral equation for the single layer operator (13) with right-hand side as in (12) is given by

$$\widehat{\varphi}_n(x,s) := \eta_n^{-1}\left(\alpha, \frac{s}{c}\right)\widehat{f}(s)\, Y_n^m(x).$$

This leads to the solution of the interior and exterior Laplace transformed wave equation (1)

$$\widehat{u}^\sigma(x,s) = \widehat{S}(s)\,\widehat{\varphi}_n(x,s) := \eta_n^{-1}\left(\alpha, \frac{s}{c}\right)\widehat{f}(s)\int_\Gamma \frac{\mathrm{e}^{-s\|x-y\|/c}}{4\pi\|x-y\|}Y_n^m d\Gamma_y \qquad \forall (x,t)\in\Omega^\sigma\times\mathbb{R}_{>0}$$

and we have to evaluate the application of the Laplace transformed single layer potential to the spherical harmonics Y_n^m. Let

$$\widehat{U}_n^m := \widehat{S}(s)\, Y_n^m.$$

[4]For $r>0$, $\mu>0$, $\beta\in\mathbb{R}$ it holds

$$\int_0^r s^\mu \mathrm{e}^{-\beta s}\, ds = \frac{\gamma(\mu+1, r\beta)}{\beta^{\mu+1}}, \tag{16}$$

where

$$\gamma(a,z) := \int_0^z t^{a-1}e^{-t}dt$$

is an incomplete Gamma function (cf. [9, 8.2.1]).

Then $\widehat{U}_n^m$ satisfies the transmission problem

$$\begin{aligned}
-\Delta\widehat{U}_n^m + \left(\frac{s}{c}\right)^2 \widehat{U}_n^m &= 0 \qquad \text{in } \mathbb{R}^3\backslash\Gamma, \\
\left[\gamma_0 \widehat{U}_n^m\right]_\Gamma &= 0 \\
\left[\gamma_1 \widehat{U}_n^m\right]_\Gamma &= -Y_n^m \\
\left|\frac{\partial\widehat{U}_n^m}{\partial r} + \frac{s}{c}\widehat{U}_n^m\right| &= o\left(r^{-1}\right) \quad r = \|\mathbf{x}\| \to \infty.
\end{aligned}$$

From [36, (2.6.53), (2.6.55)] we conclude that the solution in spherical coordinates $x = r\zeta$ with $r = \|\mathbf{x}\|$ and $\zeta \in \mathbb{S}_2$ has the form

$$\widehat{U}_n^m(x,s) = Y_n^m(\zeta) \begin{cases} \beta_n^-(s)\, j_n(\mathrm{i}sr) & 0 \le r < 1 \\ \beta_n^+(s)\, h_n^{(1)}(\mathrm{i}sr) & r > 1 \end{cases}$$

with coefficients $\beta_n^\pm$ to be determined via the transmission conditions:

$$\beta_n^-(s)\, j_n(\mathrm{i}s) = \beta_n^+(s)\, h_n^{(1)}(\mathrm{i}s) \quad \text{and} \quad \mathrm{i}s\beta_n^-(s)\, j_n'(\mathrm{i}s) - \mathrm{i}s\beta_n^+(s)\left(h_n^{(1)}\right)'(\mathrm{i}s) = 1.$$

By solving this for $\beta_n^\pm$ we end up with

$$\widehat{U}_n^m(x,s) = \rho_n\left(\frac{s}{c}, r\right) Y_n^m(\zeta) \quad \text{with} \quad \rho_n(s,r) := -s \begin{cases} h_n^{(1)}(\mathrm{i}s)\, j_n(\mathrm{i}sr) & 0 \le r \le 1, \\ j_n(\mathrm{i}s)\, h_n^{(1)}(\mathrm{i}sr) & 1 \le r. \end{cases}$$

This leads to

$$\widehat{u}^\sigma(x,s) = \eta_n^{-1}\left(\alpha, \frac{s}{c}\right) \widehat{f}(s)\, \rho_n\left(\frac{s}{c}, r\right) Y_n^m(\zeta) \qquad \forall (r\zeta, t) \in \Omega^\sigma \times \mathbb{R}_{>0}$$

For $n = m = 0$, we get

$$\rho_0(s,r) := \frac{\mathrm{e}^{-s|r-1|} - \mathrm{e}^{-s(r+1)}}{2sr}$$

so that

$$\widehat{u}^\sigma(x,s) = q_0\left(\alpha, \frac{s}{c}, r\right) \widehat{f}(s)\, Y_0^0$$

with

$$q_0(\alpha,s,r) := \frac{\rho_0(s,r)}{\eta_0(\alpha,s)} = -\frac{1}{r}\frac{\mathrm{e}^{-s|r-1|} - \mathrm{e}^{-s(r+1)}}{\sigma s(1+\alpha)+1} \sum_{\ell=0}^{\infty}\left(\frac{(s(1+\sigma\alpha)+1)\,\mathrm{e}^{-2s}}{\sigma s(1+\alpha)+1}\right)^\ell.$$

4.2.1 The Solution of the Wave Equation in Ω^+

For $\sigma = +$, we get

$$q_0(\alpha,s,r) = -\frac{1}{r}\frac{1}{s(1+\alpha)+1} \sum_{\ell=0}^{\infty}\left(\mathrm{e}^{-s(2\ell+r-1)} - \mathrm{e}^{-s(2\ell+r+1)}\right).$$

The inverse Laplace transform applied to $\widehat{u}^{+}$ can be computed by similar techniques as used for (14)

$$\mathcal{L}^{-1}\left(q_0\left(\alpha,\bullet,r\right)\right)(t) = -\frac{1}{r}\frac{1}{1+\alpha}\sum_{\ell=0}^{\infty}\Big(H\left(t-(2\ell+r-1)\right)\mathrm{e}^{-\frac{t-(2\ell+r-1)}{1+\alpha}} \\ -H\left(t-(2\ell+r+1)\right)\mathrm{e}^{-\frac{t-(2\ell+r+1)}{1+\alpha}}\Big)$$

and the exterior solution u^{+} finally is given by

$$\begin{aligned} u^{+}\left(r\zeta,t\right) &= -\frac{c}{2\sqrt{\pi}\left(1+\alpha\right)r}\left(\sum_{\ell=0}^{\left\lfloor\frac{ct-r+1}{2}\right\rfloor}\int_0^{t-\frac{2\ell+r-1}{c}}\mathrm{e}^{-\frac{c(t-\tau)-(2\ell+r-1)}{1+\alpha}}f(\tau)\,d\tau\right. \\ &\quad\left.-\sum_{\ell=0}^{\left\lfloor\frac{ct-r-1}{2}\right\rfloor}\int_0^{t-\frac{2\ell+r+1}{c}}\mathrm{e}^{-\frac{c(t-\tau)-(2\ell+r+1)}{1+\alpha}}f(\tau)\,d\tau\right) \\ &= -\frac{c}{2\sqrt{\pi}\left(1+\alpha\right)r}\mathrm{e}^{-\frac{ct-r+1}{1+\alpha}}\int_0^{t-\frac{r-1}{c}}\mathrm{e}^{\frac{c\tau}{1+\alpha}}f(\tau)\,d\tau, \end{aligned} \tag{19}$$

where we used $Y_0^0 = \left(2\sqrt{\pi}\right)^{-1}$.

Example 4.2 (bump functions (revisted)). Let $f_\upsilon(t)$ be the general bump function as in Example 4.1 and, for $r>1$, we define $\tau := ct-(r-1)$. Let $(\tau)_+ := \max\{0,\tau\}$. Then

$$u^{+}\left(r\zeta,t\right) = -\frac{\rho^{\upsilon}}{2\sqrt{\pi}\left(\rho-1\right)^{\upsilon+1}}\gamma\left(\upsilon+1,\frac{\rho-1}{1+\alpha}\tau_+\right)\frac{\mathrm{e}^{-\frac{\tau}{1+\alpha}}}{r}$$

For $f(t) = (ct)^{\upsilon}\mathrm{e}^{-ct}$ the representation of u^{+} simplifies to

$$u^{+}\left(r\zeta,t\right) = -\frac{\left(1+\alpha\right)^{\upsilon}}{2\sqrt{\pi}\alpha^{\upsilon+1}}\gamma\left(\upsilon+1,\frac{\alpha}{1+\alpha}\tau_+\right)\frac{\mathrm{e}^{-\frac{\tau}{1+\alpha}}}{r}. \tag{20}$$

The dependence of $u^{+}\left(r\zeta,t\right)$ with respect to $\alpha\geq 0$ is smooth. For $r\geq 1$, it holds

$$\left|u^{+}\left(r\zeta,t\right)\right| \leq \frac{1}{\sqrt{\pi}\left(\upsilon+1\right)\left(1+\alpha\right)}\frac{(\tau)_+^{\upsilon+1}}{1+\frac{\alpha}{1+\alpha}\tau}\frac{\mathrm{e}^{-\frac{\tau}{1+\alpha}}}{r}.$$

With increasing α the amplitude of the acoustic pressure is damped by $\frac{1}{1+\alpha}$ and the same holds for the exponent which determines the reverberation time.

Proof. By using (19) and the definition of f_υ we get

$$u^{+}\left(r\zeta,t\right) = -\frac{c}{2\sqrt{\pi}\left(1+\alpha\right)r}\mathrm{e}^{-\frac{ct-r+1}{1+\alpha}}\int_0^{t-\frac{r-1}{c}}\mathrm{e}^{-\frac{c(\rho-1)\tau}{1+\alpha}}\left(\frac{c\rho\tau}{1+\alpha}\right)^{\upsilon}d\tau.$$

1st Case: $ct \leq r-1$.
Obviously $u^{+}=0$ in this case.
2nd Case: $r-1<ct$. We employ (16) and obtain

$$u^{+}(x,t)=-\frac{\rho^{\upsilon}}{(\rho-1)^{\upsilon+1}}\mathrm{e}^{-\frac{ct-r+1}{1+\alpha}}\frac{\gamma\left(\upsilon+1,(\rho-1)\frac{ct-r+1}{1+\alpha}\right)}{2\sqrt{\pi}r}. \tag{21}$$

Next we set $\rho=1+\alpha$ so that the right-hand side becomes $f(t)=(ct)^{\upsilon}\mathrm{e}^{-ct}$ and we obtain

$$u^{+}(r\zeta,t)=\begin{cases}0 & t\leq\frac{r-1}{c},\\ -\frac{(1+\alpha)^{\upsilon}}{\alpha^{\upsilon+1}}\frac{\gamma\left(\upsilon+1,\frac{\alpha}{1+\alpha}(ct-r+1)\right)}{2\sqrt{\pi}r}\mathrm{e}^{-\frac{ct-r+1}{1+\alpha}} & t>\frac{r-1}{c}.\end{cases}$$

From [9, 8.10.2 with $a>1$ therein] we conclude that for $a\geq 1$ and $x\geq 0$ it holds

$$|\gamma(a,x)|\leq\frac{x^{a-1}}{a}\left(1-e^{-x}\right)\leq\frac{2x^{a}}{a(x+1)}.$$

For $\tau=ct-(r-1)$ and $r>1$, we have

$$\left|u^{+}(r\zeta,t)\right|\leq\frac{1}{\sqrt{\pi}(\upsilon+1)(1+\alpha)}\frac{(\tau)_{+}^{\upsilon+1}}{1+\frac{\alpha}{1+\alpha}\tau}\frac{\mathrm{e}^{-\frac{\tau}{1+\alpha}}}{r}.$$

□

5 Numerical Experiments

The purpose of this Section is to show a) how the proposed algorithm performs for model problems and b) its applicability to real-world problems. For the first goal, a systematic convergence study is presented, which utilizes the analytical solution for the sphere from Section 4. To show the applicability for real-world applications we computed the sound pressure field in the atrium of the “Institut für Mathematik” at the University Zurich with gCQ and the influence of sound absorbing material.

All boundary element computations are done in 3-D and a classical matrix-oriented spatial boundary element discretization is employed. All regular integrals are performed with Gaussian quadrature formulas. The formulas given in [12] are used for the singular integrals. The geometrical discretization is done with linear triangles and the data are approximated by piecewise linear shape functions. For the solution a direct solver is used. All implementations are done within the BE-library HyENA [34].

5.1 Unit sphere: Convergence and influence of α

The geometry chosen is a sphere with radius 1 m with a coordinate system fixed at the midpoint. The scattering into the outer air is considered and the respective analytical solutions can be found in Section 4. For the spherical harmonics in the right-hand side of (12) we choose $n=m=0$. The time behavior of the right-hand side is the discussed bump function

$$f_{\upsilon}(t)=(ct)^{\upsilon}\mathrm{e}^{-ct},$$

with $\upsilon > 0$, i.e., the analytical solutions can be found in (18) for the density and in (20) for the pressure. For all tests the material data from air are used, i.e., $c = 343\,\mathrm{m/s}$ is set. The admittance is set to $\alpha = 0.5$. In contrast to the classical CQ method, the gCQ method allows for a variable step size which becomes important to approximate solutions with singular behavior, e.g., at the initial or later times. Note that for $\upsilon \in \mathbb{R}_{>0} \backslash \mathbb{N}$ the bump function f_υ is Hölder continuous, more precisely $f_\upsilon \in C^{\lfloor \upsilon \rfloor, \{\upsilon\}}$ with $\lfloor \upsilon \rfloor$ denoting the integer part of υ and $\{\upsilon\} := \upsilon - \lfloor \upsilon \rfloor$. From (18) it follows that the non-smooth behavior of f_υ at $t = 0$ inherits qualitatively the same order of non-smoothness to the density function at time points $t_\ell = 2\ell/c$, $\ell \in \mathbb{N}_0$, i.e., $\varphi^+ \in C^{\lfloor \upsilon \rfloor, \{\upsilon\}}$. Since u_+ is defined via an integration (involved in the gamma function γ, see (20)) we conclude that $u_+ \in C^{\lfloor \upsilon \rfloor + 1, \{\upsilon\}}$.

For simplicity, we assume $\upsilon \in (0,1)$. If we want to distribute N time points in the interval $[0,T]$ such that a piecewise constant interpolation converges as $O\left(N^{-1}\right)$, the choice

$$t_n = T\left(\frac{n}{N}\right)^\chi, n = 0, \ldots, N \quad \text{with grading exponent} \quad \chi = 1/\upsilon \tag{22}$$

of the mesh points is recommended. Since we employ the BDF 1 method for the time discretization we expect an error in the approximation of the density function of $O(\Delta_{\text{const}})$ for $\Delta_{\text{const}} = T/N$. For a uniform mesh with $t_n = n\Delta_{\text{const}}$ we expect a reduced convergence order of $O\left((\Delta_{\text{const}})^\upsilon\right)$. To achieve a comparable error of $O\left(N^{-1}\right)$ for a constant mesh width one has to choose a constant time mesh with step size $\Delta_{\min} = O\left(N^{-1/\upsilon}\right)$ where $1/\upsilon > 1$.

These theoretical considerations are checked by a purely time dependent problem. The analytical solution for the density function φ^+ of the sphere (18) is compared with the approximation φ^+_Δ by the gCQ and the CQ as solution of the convolution integral

$$\int_0^t \mathcal{L}^{-1}(\eta_0)(\tau)\, \varphi^+_\Delta(t-\tau)\,\mathrm{d}\tau = f_\upsilon(t) = (ct)^\upsilon\, \mathrm{e}^{-ct}$$

where η_0 is as in (13). The CQ is evaluated following the procedure given in [4]. The value $\upsilon = 1/2$ is set for the bump function, which fits to the grading parameter $\chi = 2$. In this setting the smallest step size is approximately the square of the largest step size. In Fig. 1, the approximated and the analytical solutions are plotted versus time and, additionally, the pointwise error in time is given. Obviously, both approximate solutions and the analytical solution agree well and the error is in an acceptable range. The results have been obtained with $N = 160$ and $T = 0.003\,\mathrm{s}$. The error plot shows that the variable time step in the gCQ reduces the error at the beginning, where the solution has a non-smooth behavior. The CQ produces the largest error in the first time steps, which is larger than all errors of the gCQ.

To study the convergence behavior the maximal error defined by

$$\mathrm{err}_{\text{abs}} = \max_{1 \le n \le N} \left|\varphi^+\left(\frac{t_n + t_{n-1}}{2}\right) - \varphi^+_\Delta\left(\frac{t_n + t_{n-1}}{2}\right)\right|, \tag{23}$$

is plotted versus the time steps N in Fig. 2. The error is evaluated at the midpoint of each time step and shows the expected theoretical behavior. The order of the numerical convergence (eoc) is defined with

$$\mathrm{eoc} = \log_2\left(\frac{\mathrm{err}_\Delta}{\mathrm{err}_{\Delta+1}}\right),$$

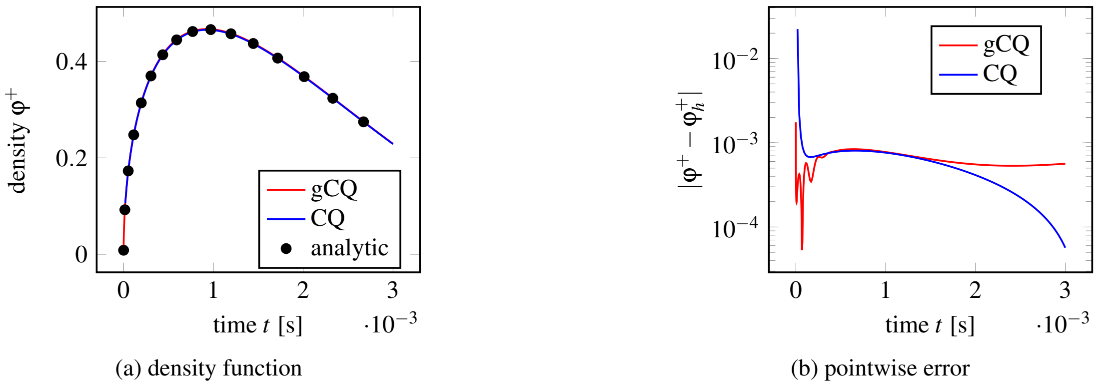

Figure 1: Comparison of gCQ- and CQ-solution for the sphere: density and error

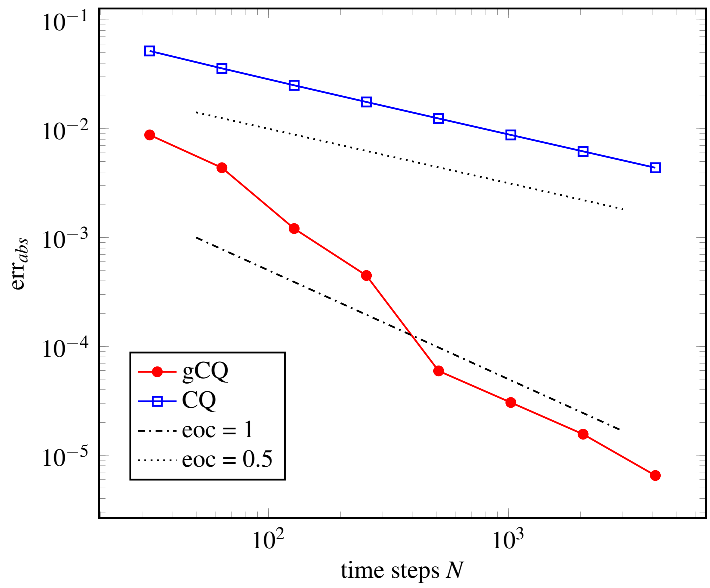

Figure 2: Maximum error for the density of the sphere

	elements	nodes	h
mesh 1	512	258	0.196 m
mesh 3	2048	1026	0.098 m
mesh 4	8192	4098	0.049 m

Table 1: Data of the refined meshes

where the indices $()_{\Delta+1}$ and $()_{\Delta}$ denotes two subsequent refinement levels. In Fig. 2, the dash-dotted line corresponds to a convergence order of one, which matches well to the gCQ-solution. The dotted line gives a convergence order of $1/2$, which matches the CQ-solution as expected.

Next, a BE-solution for the sphere is considered, i.e., additionally to the temporal discretization error a spatial discretization error is introduced. Since the space-time solution on the unit ball for the spherical harmonics Y_0^0 is spatially constant on the surface Γ (and, hence, lies in the boundary element space), the surface mesh does not introduce a spatial *discretization* error but only "variational crimes" related to spatial quadrature and surface approximation by flat panels. Hence, the total error should be dominated by the temporal discretization and the effect of numerical quadrature and surface approximation. Such a test setting may be not recommended in space-time methods as the spatial and temporal behavior of the results are coupled. Nevertheless, three different meshes and, consequently, three different geometrical approximations of the sphere are used (see Fig. 3). The triangles are uniformly refined by subdividing from mesh 1 to mesh 3. The corresponding data as element, node numbers, and respective characteristic

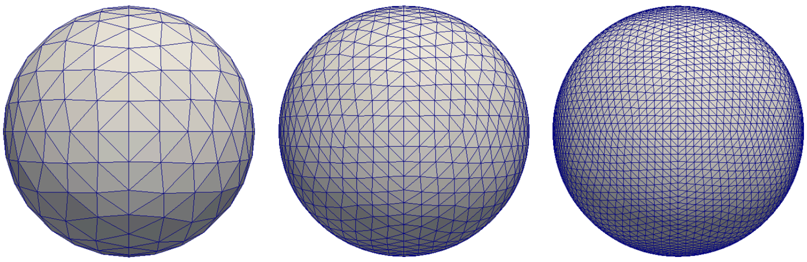

(a) mesh 1 (b) mesh 2 (c) mesh 3

Figure 3: Spatial discretisations for the sphere

element size h are given in Tab. 1. Note that the values of h are rounded. Mesh 1 consists of 32 elements on a great circle of the sphere. The total time is set to $T = 0.002915905\,\mathrm{s}$, which is approximately the inverse of the wave speed. As before, the value $\upsilon = 1/2$ is set for the bump function, which fits to the grading parameter $\chi = 2$. Hence, this numerical experiment is comparable to the above study without any BE-approximation. It is expected to see the same convergence behavior in time as in the test above. In Fig. 4, the maximal error

$$\mathrm{err}_{\mathrm{abs}} = \max_{1\leq n\leq N} ||\varphi^+\left(\frac{t_n+t_{n-1}}{2}\right) - \varphi_\Delta^+\left(\frac{t_n+t_{n-1}}{2}\right)||_{L_2}$$

is plotted versus the time steps. Note, this definition of the error differs from the definition (23) that now the L_2-norm with respect to the spatial variable is used. Overall, the same behavior as

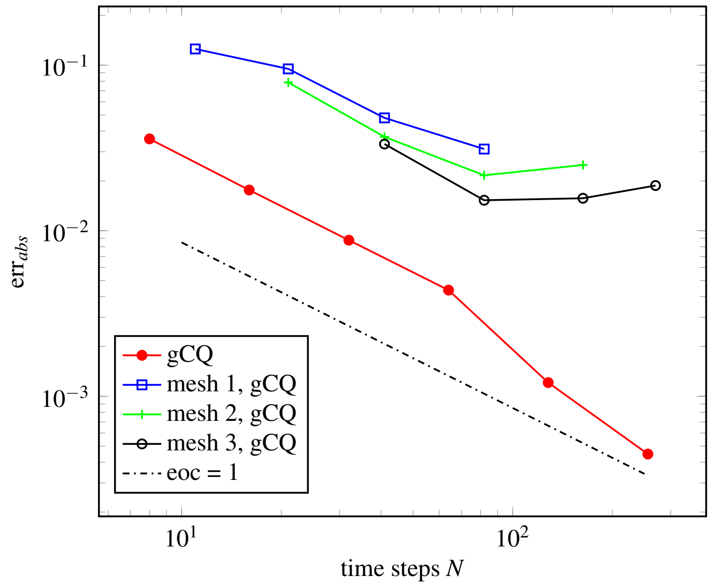

Figure 4: Error of the density versus the amount of time steps

above can be observed. The convergence order of the gCQ is linear. However, the gCQ-solutions show for larger N a drop of the error. This effects has also been observed for the gCQ-solution of the single layer potential in acoustics [27]. The reason is the spatial integration of the highly oscillatory integrals. For higher values of N higher complex frequencies have to be included in (11b). In the actual implementation only a simple distance criterium for the number of Gauss-points is used, which might be sub-optimal for the higher frequencies. Nevertheless, the results show that also the BE-solution is improved by using the gCQ for such kind of non-smooth right hand sides.

For completness, also the pressure solution is computed and the convergence behavior is studied. The pressure field is evaluated at $x = (1.5, 0, 0)^{\intercal}$, i.e. 0.5 m away of the sphere with radius of 1 m. The temporal maximal error using (23) is plotted versus the time steps in Fig. 5. The same parameters are applied as in the BE-calculation above. The error for the pressure solution shows a different behavior compared to the density. Due to the increased smoothness of the solution also an optimal convergence order is expected for the constant time mesh, which can be observed in Fig. 5. Also the level of the error of gCQ and CQ is comparable. We expect that, for stronger singularities and/or higher order discretizations, the CQ will not converge at an optimal rate while an appropriate grading of the time mesh for gCQ can preserve the optimal convergence.

After studying the convergence behavior of gCQ, the influence of the admittance α is considered. In Fig. 6, the density is plotted versus time for different values of α. We employed mesh 2 for this study and have increased the observation time to $T = 0.0125223$ s. Our grading of the time mesh might be sub-optimal for the larger final time for the computation of the density since the induced “bump” is periodically repeated in the density (cf. [40]) and, in principle, would require a mesh grading also at later times. However, the intention here is to show the qualitative

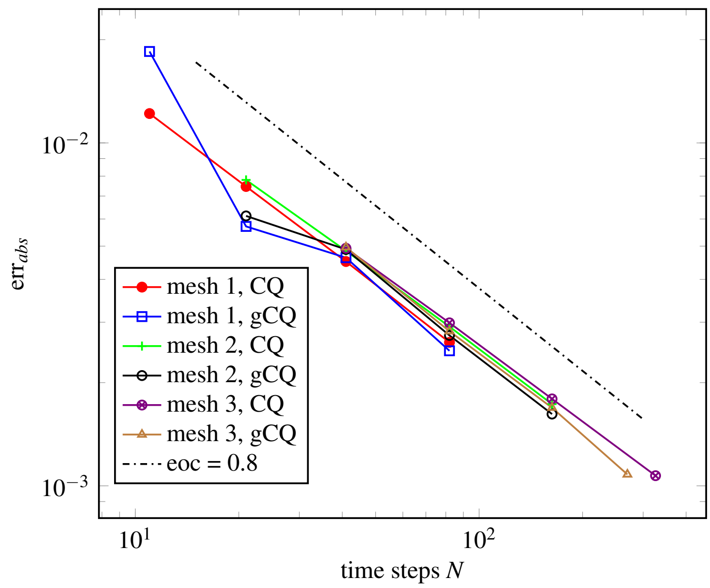

Figure 5: BEM error of the pressure versus the amount of time steps

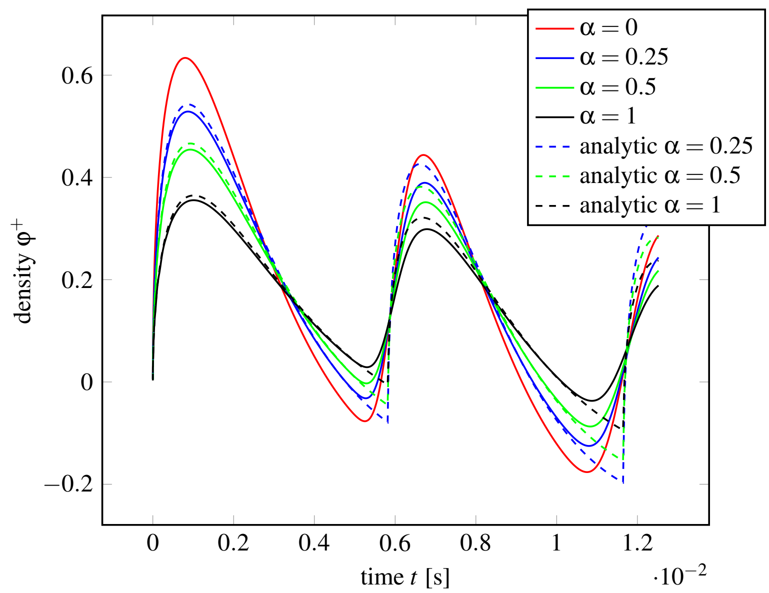

Figure 6: Density versus time for different admittances α (mesh 2)

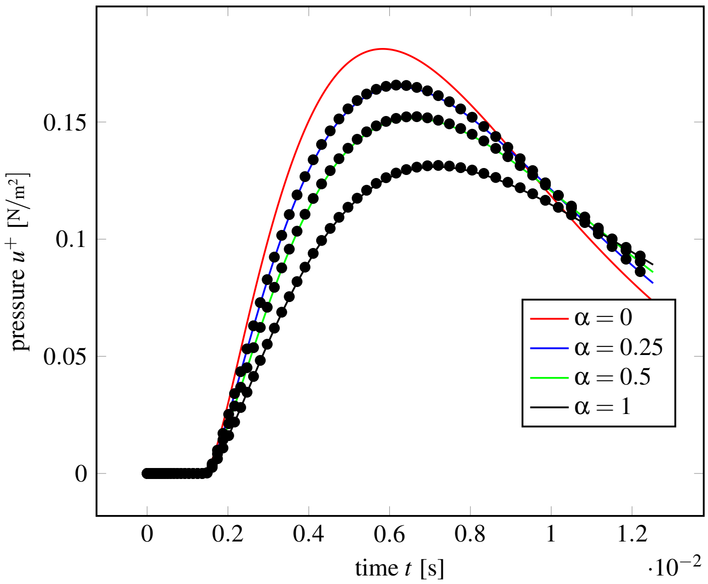

Figure 7: Pressure versus time for different admittances α (mesh 3)

influence of the admittance and this might justify a sub-optimal time grading.

As expected, the increase of the admittance results in a damping of the solution and a slower decay, where the overall qualitative behavior is similar. Besides the Galerkin boundary element solution with gCQ, the analytical solution is displayed with dashed lines. Only for $\alpha = 0$ the analytical solution is omitted as it has to be derived separately. It can be observed that the numerical solution cannot follow the peaks after the first "bump". This might be improved by using a grading of the time mesh around these times and indicates that an adaptive time mesh would be advantageous. Further, for larger times the offset to the analytical solution increases. Here the limitations of a BDF 1 as underlying time discretization becomes visible. It can be expected that with a higher order method the approximation of the density becomes better and the generalization to Runge-Kutta gCQ (cf. [26]) is the topic of future research.

Interestingly, the pressure solution is not that much influenced by this deviation of the numerical solution. In Fig. 7, the pressure is plotted versus time for the same values of α and the dots display the values of the respective analytical solution. The results match nearly perfect and the influence of the admittance is the same, it damps the solution. Theoretically this observation can be explained by the smoother behavior of the pressure compared to the density and by well known superconvergence properties of Galerkin BEM for field point evaluations. These numerical experiments confirm that the theoretical findings in Example 4.2 are sharp.

5.2 Improved acoustics in an atrium

As a realistic example the influence of absorbing layers in room acoustics is studied. In 2010/11, the atrium of the "Institut für Mathematik" at the University Zurich has been acoustically improved by installing absorber panels at the ceilings. This action has been successful and the following numerical model tries to model this effect.

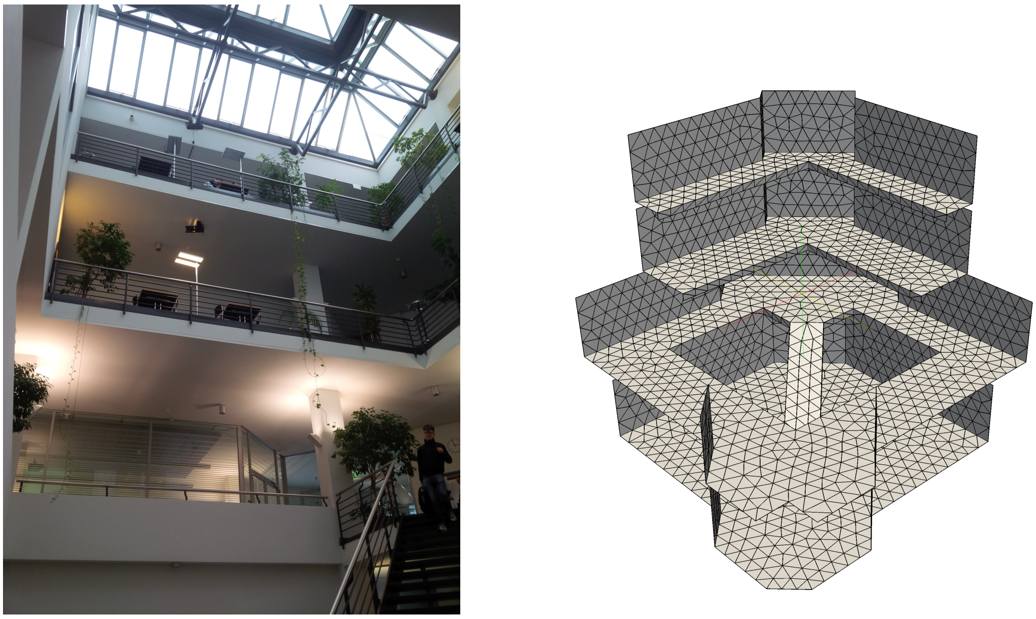

Figure 8: The atrium of the “Institut für Mathematik” at the University Zurich and the boundary element mesh. The mesh is cut such that the floors and the stair in the basement are visible.

The building is a cube where the offices are located in a ring around the atrium. In Fig. 8, a photo is shown from inside the atrium. On the down side of these floors sound absorbing material has been mounted. Clearly, the model does not include *every* detail of the geometry, e.g., the construction of the glas roof has not been modelled. However, the geometric model is fine enough, to model details such as the stair from the ground floor to the basement. This simplification allows to compute the sound pressure field in time domain at one node of our cluster (X4800 with 8 OctaCore-Intel CPU & 256GB RAM). This application shows that the proposed BE formulation is capable to treat real world problems.

The material data from air resulting in a wave speed $c = 343\,\mathrm{m/s}$ are assumed. Further, the time grading is difficult to be adjusted. In contrast to the test before the solution behavior is not known in advance and would in principle require to have an adaptive algorithm. As this is subject to further research, here, a slight modification of the grading (22) is used. A smooth increase of time steps sizes is formulated by

$$t_n = \left(n + \frac{(n-1)^2}{N} \right) \Delta_{const} \ , \tag{24}$$

which might be justified because after several reflections in this complicated geometry the solution behavior does no longer change drastically. $\Delta_{\mathrm{const}} = 0.00037\,\mathrm{s}$ is used to discretize the time interval $[0, T = 0.15\,\mathrm{s}]$ and $N = T/\Delta_{\mathrm{const}} = 405$ holds. The time grading of (24) results then in 248 time steps to be computed. Linear continuous shape functions are employed on

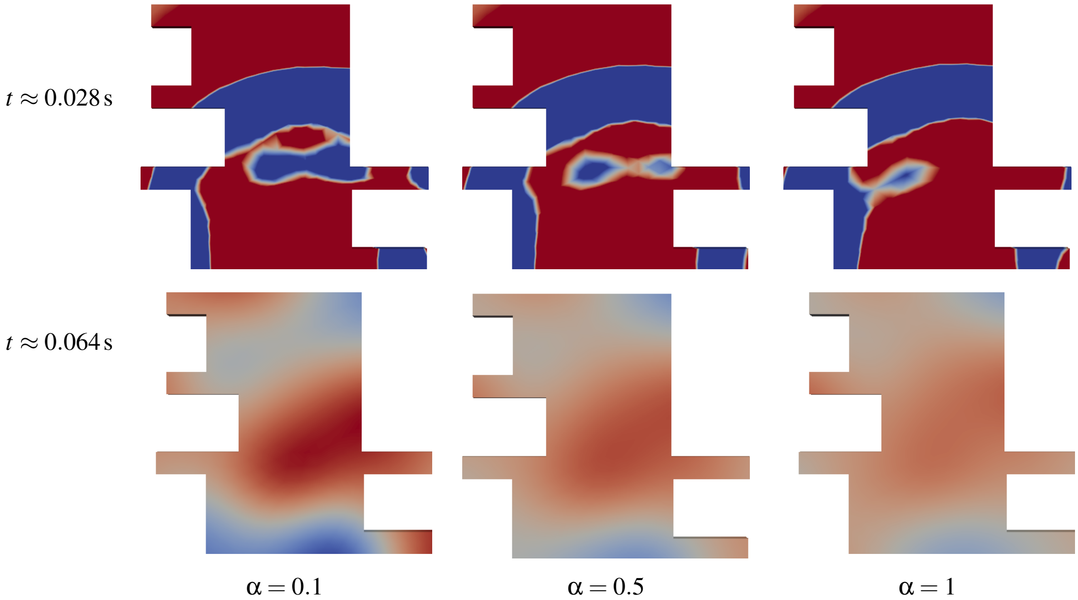

Figure 9: Sound pressure field in the atrium at different times for three different values of α

7100 flat triangles[5]. The loading is a given flux at the bottom of the stairs with a time history $f(t) = \sin(1200 \cdot t)\left(H(t) - H\left(t - \frac{2\pi}{1200}\right)\right)$. This represents a sine load with $\approx 191\,\mathrm{Hz}$ active over one period. The chosen frequency represents a mean frequency of a speaking person.

In Fig. 9, the sound pressure in the atrium displayed on a screen placed nearly in the middle of the atrium is depicted for $t \approx 0.028\,\mathrm{s}$ and $t \approx 0.064\,\mathrm{s}$ for three different materials. All walls are assumed to be nearly sound hard (e.g., made of concrete with $\alpha = 0.1$) but the down side of the floors, i.e., the ceilings visible in Fig. 8 are modelled as absorbing surfaces. The chosen α-values correspond either to no sound absorbing material ($\alpha = 0.1$), to a heavy curtain at low frequencies ($\alpha = 0.5$), and to the extreme case of totally absorbing surface ($\alpha = 1$). Note that these values are only examples and may not be the exact values for a distinct material nor the material used in reality in this atrium.

The results show clearly traveling waves in the beginning of the computation and a lot of reflections in the complicated geometry. For longer times the sound pressure level approaches a steady state with smaller values for higher damping, i.e., higher admittance. At the beginning, not much differences are visible for different values of the admittance. However, for larger observation times the sound pressure level increases as indicated by the more strong red color for the low damping material compared to the higher damping material. In Fig. 10, the sound pressure level in the upper left side of the screen is exemplarily depicted over time. Note, the sound pressure level is given in dB and negative values indicate sound below the threshold of hearing. Further, the initial phase where the pressure is zero, i.e., the time until the wave arrives, is truncated as in this case the dB measure gives very large negative values. In this plot two

[5]The geometry and the mesh have been generated by Dominik Pölz (Graz University of Technology) during his master thesis at the Institute of Applied Mechanics.

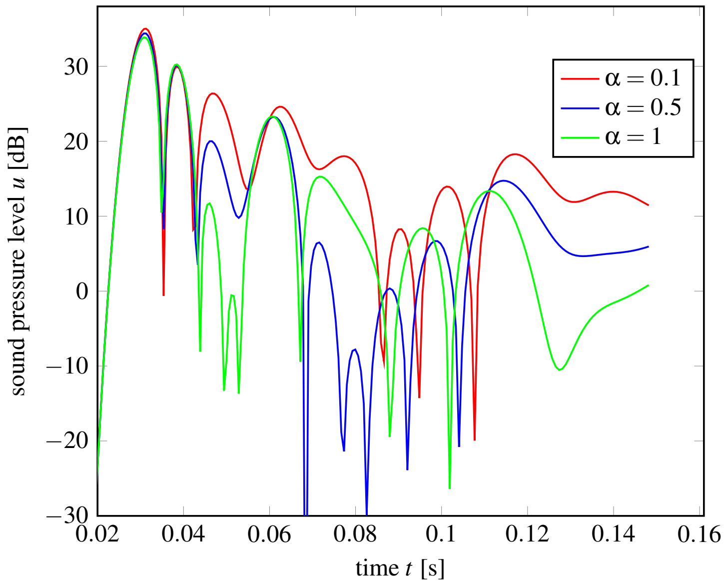

Figure 10: Sound pressure level in dB versus time in the upper left part of the observation screen

things can be observed. First, the peaks with the negative values show the wave reflections, which arrive for the different damping cases at different times. Second, the sound pressure for $\alpha = 0.1$, i.e. no mounted damping material, has in the mean the larger pressure values. The two other cases show that the damping material can reduce the sound pressure level as reported from the real building, where it is claimed that the atrium is no longer such noisy. Certainly, the effect is different at different locations within the atrium.

6 Conclusions

Impedance boundary conditions are very natural in acoustic calculations. They constitute a Robin type boundary condition, which can be treated easily with retarded potential integral equations. However, for impedance boundary conditions the time derivative of the Dirichlet part is combined with the Neumann part. The application of the convolution quadrature (CQ) method as time discretization for this problem is straightforward. Here, the generalized form of the CQ the gCQ is applied, which allows for a non-uniform time mesh in contrast to the original CQ method.

For a spherical scatterer, analytical solutions are derived, which are given explicitly for the scattering problem and zero order Hankel functions as spatial right-hand side. In general, the time behavior can be expressed via a time integral while, for a “bump-function”, explicit expressions are presented. These solutions are used to study systematically the convergence behavior of the proposed algorithm with respect to the time discretization. The results show the expected rates. For non-smooth time behavior the gCQ is superior to a constant time mesh as expected. An open question at this point is the optimal grading of the time mesh for more general right-hand sides. Future research will elaborate on adaptivity in time, while the gCQ allows for a straightforward algorithmic realization.

Finally, a real world example has been studied. The interior sound field in the atrium of the "Institut für Mathematik"at the University Zurich has been calculated for different sound absorbing materials at the ceilings. The calculations show that the proposed method is suitable to compute such a real world application. Certainly, so-called fast methods can improve the performance of the presented formulation.

Acknowledgement The second author gratefully acknowledges the hospitality and support by the "Institut für Mathematik" at the University Zurich during his sabbatical leave.

References

[1] B. Alpert, L. Greengard, and T. Hagstrom. Rapid evaluation of nonreflecting boundary kernels for time-domain wave propagation. *SIAM J. Numer. Anal.*, 37(4):1138–1164, 2000.

[2] A. Bamberger and T. Ha-Duong. Formulation variationelle espace-temps pour le calcul par potentiel retardé d'une onde acoustique. *Math. Meth. Appl. Sci.*, 8:405–435 and 598–608, 1986.

[3] L. Banjai and A. Rieder. Convolution quadrature for the wave equation with a nonlinear impedance boundary condition. *ArXiv e-prints*, April 2016.

[4] L. Banjai and S.A. Sauter. Rapid solution of the wave equation in unbounded domains. *SIAM J. Numer. Anal.*, 47(1):227–249, 2008.

[5] Lehel Banjai, Christian Lubich, and Jens Markus Melenk. Runge-Kutta convolution quadrature for operators arising in wave propagation. *Numer. Math.*, 119(1):1–20, 2011.

[6] J. Thomas Beale and Steven I. Rosencrans. Acoustic boundary conditions. *Bull. Amer. Math. Soc.*, 80:1276–1278, 1974. ISSN 0002-9904.

[7] Jean-Pierre Berenger. A perfectly matched layer for the absorption of electromagnetic waves. *J. Comput. Phys.*, 114(2):185–200, 1994.

[8] H. Diao. *Adaptive Convolution Quadrature for the Wave Equation*. PhD thesis, Inst. f. Mathematik, Universität Zürich, 2017.

[9] DLMF. NIST Digital Library of Mathematical Functions. http://dlmf.nist.gov/, Release 1.0.9 of 2014-08-29. URL `http://dlmf.nist.gov/`. Online companion to [37].

[10] Bjorn Engquist and Andrew Majda. Absorbing boundary conditions for the numerical simulation of waves. *Math. Comp.*, 31(139):629–651, 1977.

[11] A. Erdélyi, W. Magnus, F. Oberhettinger, and F. G. Tricomi. *Tables of integral transforms. Vol. I.* McGraw-Hill Book Company, Inc., New York-Toronto-London, 1954. Based, in part, on notes left by Harry Bateman.

[12] S. Erichsen and S. A. Sauter. Efficient automatic quadrature in 3-d Galerkin BEM. *Comput. Methods Appl. Mech. Engrg.*, 157(3–4):215–224, 1998.

[13] Silvia Falletta, Giovanni Monegato, and Letizia Scuderi. A space-time BIE method for nonhomogeneous exterior wave equation problems. The Dirichlet case. *IMA J. Numer. Anal.*, 32(1):202–226, 2012.

[14] M. Filipe, A. Forestier, and T. Ha-Duong. A time dependent acoustic scattering problem. In *Mathematical and numerical aspects of wave propagation (Mandelieu-La Napoule, 1995)*, pages 140–150. SIAM, Philadelphia, PA, 1995.

[15] Andreas Franck and Marc Aretz. Wall structure modeling for room acoustic and building acoustic fem simulations. In *Proc. of 19th International Congress on Acoustics*, 2007.

[16] M.B. Friedman and R.P. Shaw. Diffraction of Pulses by Cylindrical Obstacles of Arbitrary Cross Section. *J. Appl. Mech.*, 29:40–46, 1962.

[17] P. Jameson Graber. Uniform boundary stabilization of a wave equation with nonlinear acoustic boundary conditions and nonlinear boundary damping. *J. Evol. Equ.*, 12(1):141–164, 2012. ISSN 1424-3199. doi: 10.1007/s00028-011-0127-x. URL `http://dx.doi.org/10.1007/s00028-011-0127-x`.

[18] Marcus J. Grote and Imbo Sim. Local nonreflecting boundary condition for time-dependent multiple scattering. *J. Comput. Phys.*, 230(8):3135–3154, 2011.

[19] T. Ha-Duong. On Retarded Potential Boundary Integral Equations and their Discretization. In M. Ainsworth, P. Davies, D. Duncan, P. Martin, and B. Rynne, editors, *Computational Methods in Wave Propagation*, volume 31, pages 301–336, Heidelberg, 2003. Springer.

[20] T. Ha-Duong, B. Ludwig, and I. Terrasse. A Galerkin BEM for transient acoustic scattering by an absorbing obstacle. *Int. J. Numer. Meth. Engng*, 57:1845–1882, 2003.

[21] W. Hackbusch, W. Kress, and S. Sauter. Sparse convolution quadrature for time domain boundary integral formulations of the wave equation by cutoff and panel-clustering. In M. Schanz and O. Steinbach, editors, *Boundary Element Analysis: Mathematical Aspects and Applications*, volume 18, pages 113–134. Springer Lecture Notes in Applied and Computational Mechanics, 2006.

[22] Thomas Hagstrom and S. I. Hariharan. A formulation of asymptotic and exact boundary conditions using local operators. *Appl. Numer. Math.*, 27(4):403–416, 1998.

[23] R. Kress. Minimizing the Condition Number of Boundary Integral Operators in Acoustics and Electromagnetic Scattering. *Q. Jl. Mech. appl. Math.*, 38:323–341, 1985.

[24] Antonio R. Laliena and Francisco-Javier Sayas. Theoretical aspects of the application of convolution quadrature to scattering of acoustic waves. *Numer. Math.*, 112(4):637–678, 2009.

[25] M. Lopez-Fernandez and S. Sauter. Fast and stable contour integration for high order divided differences via elliptic functions. *Math. Comp.*, 84(293):1291–1315, 2015.

[26] M. Lopez-Fernandez and S. Sauter. Generalized Convolution Quadrature based on Runge-Kutta Methods. *Numer. Math.*, 133(4):743–779, 2016. ISSN 0029-599X. doi: 10.1007/s00211-015-0761-2. URL http://dx.doi.org/10.1007/s00211-015-0761-2.

[27] Maria Lopez-Fernandez and Stefan Sauter. Generalized convolution quadrature with variable time stepping. Part II: Algorithm and numerical results. *Appl. Numer. Math.*, 94: 88–105, 2015.

[28] Maria Lopez-Fernandez and Stefan A. Sauter. Generalized Convolution Quadrature with Variable Time Stepping. *IMA J. Numer. Anal.*, 33(4):1156–1175, 2013.

[29] C. Lubich. Convolution quadrature and discretized operational calculus I. *Numer. Math.*, 52:129–145, 1988.

[30] C. Lubich. Convolution quadrature and discretized operational calculus II. *Numer. Math.*, 52:413–425, 1988.

[31] C. Lubich. On the multistep time discretization of linear initial-boundary value problems and their boundary integral equations. *Numer. Math.*, 67:365–389, 1994.

[32] C. Lubich. Convolution quadrature revisited. *BIT Numerical Mathematics*, 44:503–514, 2004.

[33] Ch. Lubich and A. Ostermann. Runge-Kutta methods for parabolic equations and convolution quadrature. *Math. Comp.*, 60(201):105–131, 1993.

[34] Ma. Messner, Mi. Messner, F. Rammerstorfer, and P. Urthaler. Hyperbolic and elliptic numerical analysis BEM library (HyENA). http://www.mech.tugraz.at/HyENA, 2010. [Online; accessed 22-January-2010].

[35] L. Nagler, P. Rong, M. Schanz, and O. v. Estorff. Sound transmission through a poroelastic layered panel. *Comput. Mech.*, 53(4):549–560, 2014. doi: 10.1007/s00466-013-0916-x.

[36] J. C. Nédélec. *Acoustic and Electromagnetic Equations*. Springer, New York, 2001.

[37] F. W. J. Olver, D. W. Lozier, R. F. Boisvert, and C. W. Clark, editors. *NIST Handbook of Mathematical Functions*. Cambridge University Press, New York, NY, 2010. Print companion to [9].

[38] S. Sauter and A. Veit. Retarded Boundary Integral Equations on the Sphere: Exact and Numerical Solution. *IMA J. Numer. Anal.*, 34(2):675–699, 2013.

[39] S. Sauter and A. Veit. A Galerkin Method for Retarded Boundary Integral Equations with Smooth and Compactly Supported Temporal Basis Functions. *Numer. Math.*, 123:145–176, 2013.

[40] S. Sauter and A. Veit. Adaptive Time Discretization for Retarded Potentials. *Numer. Math.*, 132(3):569–595, 2016.

[41] Francisco-Javier Sayas. *Retarded Potentials and Time Domain Boundary Integral Equations: A Road Map*. Springer Verlag, 2016.

[42] E. P. Stephan, M. Maischak, and E. Ostermann. Transient Boundary Element Method and Numerical Evaluation of Retarded Potentials. In M. Bubak, G.D. van Albada, J. Dongarra, and P.M.A. Sloot, editors, *Computational Science – ICCS 2008, LNCS, 5102*, pages 321–330, Heidelberg, 2008. Springer.

[43] J.A. Stratton. *Electromagnetic Theory*. McGraw-Hill, New York, 1941.

[44] A. Veit. *Numerical Methods for Time-Domain Boundary Integral Equations*. PhD thesis, Inst. f. Math., Universität Zürich, 2012.